



Contents lists available at ScienceDirect

Environmental Technology & Innovation

journal homepage: www.elsevier.com/locate/eti

An efficient biosynthesis of novel ZnO/CuO nanocomposites using *berberis vulgaris* extract (ZnO/CuO@BVENCs) for enhanced photocatalytic degradation of pollution, antibacterial and antifungal activity

Ali Yousefinia^{a,1}, Maryam Khodadadi^{b,1}, Sobhan Mortazavi-Derazkola^{c,*}^a Student Research Committee, Birjand University of Medical Sciences, Birjand, Iran^b Department of Environmental Health Engineering, Birjand University of Medical sciences, Birjand, Iran^c Medical Toxicology and Drug Abuse Research Center (MTDRC), Birjand University of Medical Sciences, Birjand, Iran

ARTICLE INFO

Article history:

Received 1 July 2023

Received in revised form 10 August 2023

Accepted 16 August 2023

Available online 22 August 2023

Keywords:

Green synthesis

CuO

ZnO

Antibacterial

Antifungal

Photocatalyst

ABSTRACT

In this study, an environmentally-friendly method was employed to synthesize ZnO/CuO nanocomposites using *berberis vulgaris* extract, resulting in ZnO/CuO@BVE NCs. The structure and properties of the ZnO/CuO@BVE NCs were characterized using various analytical techniques including XRD, UV-DRS, FESEM, FT-IR, EDAX, and TEM. UV-DRS results highlighted a bandgap energy reduction from 3.11 eV to 2.93 eV due to CuO integration with ZnO. TEM images confirmed the nanocomposite size to be between 35–50 nm. To evaluate the photocatalytic effectiveness of the biosynthesized nanocomposites, rhodamine b (RhB) was used as a representative contaminant. We thoroughly investigated the influence of multiple variables such as dye concentration, nanocatalyst amount, light source, and pH on the photocatalytic degradation of RhB. Under optimized conditions (0.15 g/L nanocatalyst, pH 11, UV light, and 3 ppm pollutant concentration), a remarkable 97.3% RhB degradation efficiency was achieved. Additionally, the antibacterial properties of the ZnO/CuO@BVE NCs were tested against six ATCC strains. Notably, they exhibited strong antibacterial action, especially against *K. pneumoniae* and *P. aeruginosa*, with a minimum inhibitory concentration (MIC) as low as 62.5 µg/mL. Furthermore, the nanocomposites demonstrated significant antifungal activity against *C. albicans* with an MIC of 31.2 µg/mL. This research emphasizes the potential applications of ZnO/CuO@BVE NCs in environmental remediation and medical fields.

© 2023 The Author(s). Published by Elsevier B.V. This is an open access article under the CC BY-NC-ND license (<http://creativecommons.org/licenses/by-nc-nd/4.0/>).

1. Introduction

In the contemporary era, the depletion of water resources underscores the critical significance of addressing a wide spectrum of environmental contaminants. The contamination of water bodies by organic pollutants poses a significant threat to the viability of aquatic ecosystems while also elevating the risk of cancer in human populations. Diverse industries including plastic, paper, leather, and textiles utilize an extensive array of over a hundred thousand distinct dye variants (Abdussalam-Mohammed et al., 2020; Wang et al., 2011). Recent findings underscore that the global production of

* Corresponding author.

E-mail address: S.mortazavi23@yahoo.com (S. Mortazavi-Derazkola).

¹ These authors contributed equally to this work.

assorted organic dyes exceeds 700,000 tons, catering to various applications, yet a substantial portion of their byproducts are released into the environment without proper treatment protocols. The apprehension surrounding the presence of an extensive assortment of hazardous organic pollutants, often with uncertain concentrations, within water sources has gained substantial traction. These intricate organic compounds exhibit remarkable persistence in aquatic environments due to their complex and protracted molecular structures (Hu et al., 1987). Among these deleterious substances, Rhodamine B stands out as a noteworthy cationic dye, notorious for its adverse impacts on both the environment and living organisms (Sadeghi et al., 2020).

Multiple techniques, including chemical precipitation and surface absorption, have been employed to mitigate the presence of contaminants in water sources, driven by the adverse impact of heavy metals and chemical toxins on the ecosystem (Bader et al., 2018; Chong et al., 2010; Sun et al., 2016). Among these strategies, the application of photocatalysts stands out as a prevalent approach for remediating water environments (Huang et al., 2011). Photocatalysis, serving as a potent tool, facilitates the transformation of hazardous waste materials, particularly organic compounds, into less harmful entities (Baldez et al., 2008). Consequently, the utilization of photocatalytic processes for the extraction of waste materials has gained widespread acceptance and utility. In recent years, nanotechnology has played a pivotal role in addressing environmental challenges. Numerous scientists have engineered diverse nanomaterials and examined their impact on various pollutants. Several of these nanomaterials have exhibited remarkable efficacy in mitigating pollutants. Among these pioneering substances are Ag (Hashemi et al., 2022), Au (Roya Alizadeh et al., 2023), Bi₂S₃-TiO₂ (Sarentuya et al., 2023), ZnO-Ag (Fouladi-Fard et al., 2022), rGO-NiO/CdO (Ceril Jeoffrey et al., 2023), and MnFe₂O₄/BiOI (Golrizkhatami et al., 2023).

Zinc oxide (ZnO) stands as an inorganic compound with semiconductor properties, commonly employed as a photocatalyst across diverse industries due to its environmental compatibility. Earlier studies have showcased the exceptional photocatalytic activity exhibited by zinc oxide nanoparticles. Furthermore, recent research has illuminated that coating of zinc oxide nanostructures with another appropriate semiconductor materials can engender composite material with properties superior to those of pure zinc oxide (Khan et al., 2011; Li and Haneda, 2003; Zeng et al., 2013). Notably, copper oxide (CuO) emerges as a particularly suitable semiconductor for enhancing photocatalytic efficiency, owing to its remarkable functional attributes in comparison to other semiconductors. CuO, functioning as a p-type semiconductor, possesses a crystalline structure and maintains a band gap of 1.2 eV at room temperature. Exploiting its elevated optical absorption coefficient, alongside high electrical and thermal conductivity, positions copper oxide as an exemplary candidate for diverse applications (Filipič and Cvelbar, 2012). The fabrication of copper oxide has been realized through multiple approaches, including precipitation, sol-gel, and thermal evaporation techniques (Huang et al., 2004; Lillo-Ramiro et al., 2021; Parekh et al., 2021). The amalgamation of ZnO with a semiconductor like CuO engenders the creation of a p-n junction. This junction not only amplifies photon absorption but also significantly enhances photocatalytic performance beyond what can be achieved by the individual zinc oxide or copper oxide compounds alone (Senthil Kumar et al., 2017; Zhu et al., 2018).

Barberry, a plant native to Europe and Asia and notably found in Iran's South Khorasan Province, has been utilized in traditional medicine due to its various components such as roots, leaves, and fruits. It is renowned for its antioxidant, anti-inflammatory, anti-tumor, and antibacterial properties (Hoshyar et al., 2016; Imenshahidi and Hosseinzadeh, 2016). This plant has historical applications in treating conditions like jaundice, cholecystitis, leishmaniasis, kidney stones, malaria, dysentery, and gallstones (Anzabi, 2018). The plant contains significant chemical compounds, including berbamine, palmatine, and berberine alkaloids, known for their notable regenerative capabilities (Srivastava et al., 2015). Furthermore, other compounds such as glucoside, stigmaterol, lupeol terpenoids, and oleanolic acid contribute to its chemical composition. An intriguing aspect of barberry is its potential as a natural masking agent (Hermenean et al., 2012). This property makes it a promising alternative to chemical surfactants, aiding in achieving consistent and uniform compositions. In the context of this study, the focus shifts to utilizing barberry as a masking agent in the synthesis of ZnO/CuO@BVE NCs. This choice aligns with environmental concerns, replacing potentially harmful chemical agents with a locally sourced, eco-friendly solution from the South Khorasan province.

This study marks the inaugural utilization of *Berberis vulgaris* extract in the production process of CuO-doped ZnO. The synthesized nanoparticles underwent a series of analyses encompassing FESEM, XRD, FT-IR, TEM, and EDAX. The photocatalytic degradation efficiency of the ZnO/CuO@BVE NCs was evaluated for the purpose of rhodamine B removal. Furthermore, the antifungal and antibacterial efficacies of the ZnO/CuO@BVE NCs were assessed. This research introduces several novel aspects, enhancing its significance and impact: (i) Eco-Friendly Synthesis Approach: A distinctive aspect is the adoption of an environmentally conscious and cost-effective method for producing ZnO/CuO@BVE NCs. This departure from conventional synthesis methods contributes to sustainability and resource efficiency. (ii) Native Coating Agent: The utilization of *Barberry vulgaris* extract sourced from the South Khorasan province of Iran as a natural coating agent represents an innovative approach. This organic agent facilitates the creation of consistent and uniform nanocomposites, highlighting the potential of local resources in advanced material development. (iii) Broad-Spectrum Antibacterial Efficacy: The research showcases notable antibacterial activity against both Gram-positive and Gram-negative strains. This balanced efficacy against diverse bacterial types underscores the potential applicability of the synthesized nanocomposites in various antibacterial applications. (iv) Efficiency Optimization: By meticulously studying the impact of various parameters such as pH, nanocatalyst dose, and pollutant dose, the research offers a comprehensive understanding of factors influencing pollutant degradation efficiency. This optimization approach enhances the practical utility of the nanocomposites in real-world applications. (v) Enhanced Pollutant Degradation: The remarkable efficiency demonstrated in degrading Rhodamine B, a prevalent pollutant, underscores the practical significance of the synthesized nanocomposites. This impressive degradation performance indicates their potential in addressing pollution-related challenges.

2. Experimental

2.1. Chemical used

Zn(NO₃)₂·6H₂O, sodium dodecyl benzene sulfonate (SDBS), Cu(NO₃)₂·6H₂O and rhodamine B were purchase from Sigma Aldrich Company. For antibacterial and antifungal activities, six standard strains were applied. These included three species of Gram-positive and three Gram-negative bacteria. *Candida albicans* (*C. albicans*) was used to investigate antifungal activity

2.2. Preparation of berberis vulgaris extract

The extraction process was carried out using Shirzadi and colleagues method with a minor modification (Shirzadi-Ahodashi et al., 2021). Initially, a specimen of *Berberis vulgaris* was collected from Birjand, located in South Khorasan province. The sample was then identified and confirmed by a plant systematics expert. Next, 30 grams of the plant were ground using a grinder and turned into a powder. Following this, the plant powder was soaked in a methanol solution for 72 h. After this period, the mixture was filtered, and the solvent was removed using a rotary machine.

2.3. Zinc oxide

Pure ZnO NPs were fabricated using a precipitation route. For a standard experiment, 2 g of zinc salt was dissolved in 30 ml of distilled at 50 °C. Subsequently, 0.9 g of SDBS (with a molar ratio of Zn to SDBS as 1:1) was added to a solution of distilled water (20 ml), and this mixture was then introduced into the previous solution while vigorously stirring. The pH of the reaction was adjusted to 12 (using 25% w/w NH₃⁺). The resulting milky precipitate was separated through centrifugation, washed multiple times, and then dried. The obtained precipitate was subjected to calcination at 500 °C for 3 h.

2.4. ZnO/CuO nanocomposites

To synthesize the ZnO/CuO@BVE NCs, the previous method was utilized with certain modification (Meena et al., 2021). Initially, 1 g of the pure ZnO NPs prepared in the previous step was dispersed in 30 ml of distilled water under ultrasonic conditions for 30 min. Following this, 1.9 g of copper nitrate salt was dissolved in 15 ml of distilled water. Gradually, 8 ml of *berberis vulgaris* extract was gradually added to the copper solution. The resulting mixture was then slowly introduced into the dispersed ZnO solution. NaOH was added to the solution to achieve a pH of 12. The resulting precipitate was washed three times, subjected to centrifugation (to remove any residual reactants), and then dried for 24 h. Finally, the precipitate was calcined at 450 °C for 3 h (Shokraiyani et al., 2021).

2.5. Photocatalytic decomposition

To investigate the photocatalytic performance of ZnO/CuO@BVE NCs, experiments were conducted using both UV and sunlight irradiations. Organic dye with a concentration of 10 mg/l was dissolved in 200 ml of distilled water. A specific amount of the prepared nanocomposites was dissolved in a designated volume of water and added to the rhodamine b solution, ensuring proper dispersion. The solution was then incubated for 30 min before being exposed to UV-400 light irradiation. Samples were taken at specific time intervals during the reaction, and the concentration of the pollutant was measured at approximately 540 nm. To determine the optimal conditions for degrading rhodamine b, an experimental design was implemented by varying key factors. These factors included pH levels (ranging from 3 to 11), dye concentration (3, 5, and 10 ppm), light sources (UV and sunlight), and catalyst dosage (0.05, 0.1, 0.15, and 0.2 g/l). By adjusting these parameters, the ideal conditions for achieving the highest decomposition of rhodamine b could be identified. The percentage of pollutant decomposition was determined using Eq. (1): $D (\%) = (C_0 - C_t)/C_0 * 100$ (Eq. (1)), where C_0 represents the initial absorption and C_t is the absorption at a given time t . The kinetics of the catalytic decomposition of rhodamine b was tested, with a focus on the Langmuir-Hinshelwood model (Eq. (2)) which is commonly used for photocatalytic reactions (Ollis, 2018). The model involves the reaction rate (r) being equal to the product of the rate constant of the photocatalytic process (k) and the pollutant concentration (C), divided by the sum of one and the absorption rate constant (K). At low concentrations, the value of KC is insignificant in comparison to one ($KC < 1$), indicating that the reaction rate is of the first order (Eq. (3)).

$$r = -\frac{dc}{dt} = \frac{kKC}{1 + KC} \quad (1)$$

$$-\ln\left(\frac{C}{C_0}\right) = K_{app}t \quad (2)$$

Where C_0 is the initial concentration of the organic pollutant, t is the time and K_{app} is the apparent speed constant.

2.6. Antifungal and antibacterial activity

The research aimed to assess the effectiveness of the synthesized ZnO/CuO@BVE NCs against six bacterial strains and one type of fungus. To compare the effects of the synthesized nanoparticles with antibiotics and antifungal drugs, ceftriaxone and amphotericin B were employed. For the experimental setup, various concentrations of ZnO/CuO@BVE NCs (2000, 1000, 500, 125, 62.5, and 31.25 $\mu\text{g}/\text{mL}$), along with amphotericin B and ceftriaxone, were added to sterile microplate wells. To achieve the McFarland standard of 0.5, a specific volume of Muller Hinton Broth (MHB) culture medium containing a microbial suspension was introduced to the wells. Both positive control and negative control wells were designated. After 24 h, the turbidity of the wells was assessed to determine the minimum inhibitory concentration (MIC). To ensure robust and reliable results, the entire procedure was repeated thrice, ensuring the validity of the findings.

2.7. Characterization

X-ray diffraction (XRD) analysis was conducted using a Philips PW 1800 instrument with monochromatic Cu K α radiation ($\lambda = 1.54 \text{ \AA}$). The shape of the nanomaterials was characterized through field emission scanning electron microscope (FESEM) using a Zeiss-EM10C-100 KV instrument, as well as transmission electron microscopy (TEM) with a Zeiss-EM10C-100 KV instrument. Zeta potential and size distribution values of the samples were determined using dynamic light scattering (DLS) via a NanoBrook 90Plus instrument (model 18051) from Brookhaven. The Fourier transform infrared (FT-IR) spectra were acquired using a PerkinElmer Spectrum Two™ spectrometer (Model L160000U) in a KBr pellet configuration, covering the wavelength range of 400–4000 cm^{-1} .

3. Results and discussion

3.1. XRD, FT-IR and TEM

The crystalline and structural characteristics of both pure ZnO and ZnO/CuO@BVE NCs, synthesized through biological process were analyzed with XRD pattern, as shown in Fig. 1a. The XRD analysis revealed reflection peaks corresponding to crystallographic planes (100), (002), (101), (102), (110), (103), (112), (201), and (004) for pure ZnO nanoparticles, which were observed at 2θ angles of 32.15° , 34.39° , 36.44° , 47.51° , 56.73° , 63.36° , 48.05° , 69.15° , and 78.33° respectively. This pattern indicated a hexagonal wurtzite crystal structure for the pure ZnO nanoparticles, consistent with the JCPDS card number 01-080-0075. The XRD pattern obtained from the ZnO nanoparticles was in agreement with the findings reported by Zaimbashi et al. (Zaimbashi et al., 2022). In their study, Zaimbashi and his colleagues also utilized hydrothermal route for the fabrication of ZnO NPs. The XRD pattern of the ZnO/CuO NCs, synthesized using *berberis vulgaris* extract, is illustrated in Fig. 1a. Upon deposition of CuO onto the surfaces of ZnO nanoparticles, four additional diffraction peaks emerged at 35.17° , 38.79° , 48.15° , 67.42° , and 72.91° , corresponding to the (-111) , (111) , (-202) , (220) , and (311) planes of CuO (JCPDS card number 01-080-1268), respectively. The appearance of these diffraction peaks associated with CuO confirms the successful synthesis of ZnO/CuO@BVE NCs. Amna Iqbal et al. employed a green chemistry approach to synthesize copper oxide nanoparticles. Their result was matched with our study results (Nagajyothi et al., 2017). The XRD pattern prominently reveals that the zinc oxide peaks exhibit greater intensity, indicating higher abundance and enhanced crystallinity of zinc oxide nanoparticles within the ZnO/CuO@BVE NCs framework. Correspondingly, due to their lower prevalence (CuO) on the zinc oxide nanoparticles, the copper oxide nanoparticles' intensity in the XRD pattern remains comparatively subdued. Our findings align with the outcomes reported by Cao et al. who synthesized ZnO–CuO nanoparticles employing *Sambucus nigra* L. extract (Cao et al., 2021). The XRD pattern obtained from the synthesized ZnO/CuO@BVE NCs corresponds well with the findings in their study. The size of the synthesized nanocomposites through biological process was determined using the Debye–Scherrer equation (Khormali et al., 2021). Applying this equation, the size of the pure ZnO NPs and ZnO/CuO@BVE NCs was calculated to be 27 nm and 46 nm, respectively.

To determine the functional groups and their characteristic peak values, FTIR analysis was employed to identify the synthesis of ZnO NPs and ZnO/CuO@BVE NCs. The spectra obtained from this analysis are depicted in Fig. 1b. The FTIR spectra of pure ZnO nanoparticles exhibit O–H stretch vibrations, C–H vibrations, and a metal–oxygen (Zn–O) band at 3412, 2963, and 608 cm^{-1} , respectively (Nguyen et al., 2020). Additionally, copper oxide nanoparticles display three distinctive absorption bands at 596 and 617 cm^{-1} (Jafarirad et al., 2016; Jayaprakash et al., 2015). A band at 3408 cm^{-1} corresponds to the hydroxyl stretching mode vibration. The FT-IR analysis of ZnO/CuO@BVE NCs unveils characteristic IR absorption bands associated with both ZnO and CuO materials. These findings confirm the successful formation of zinc–oxygen and copper–oxygen bonds in the ZnO/CuO@BVE NCs. The deposition of copper oxide onto zinc oxide leads to a reduction in the IR absorption bands in the range of 1000–4000 cm^{-1} for the as-prepared ZnO/CuO@BVE NCs (Lv et al., 2021).

TEM and HR-TEM analysis were employed for a more precise determination the size and shape of the synthesized nanocomposites. Fig. 1c and d illustrate TEM images of ZnO and ZnO/CuO@BVE NCs, respectively. From the images, it is evident that the shape of ZnO nanoparticles is primarily spherical, with some particles having a slightly oval appearance. Moreover, the prevailing morphology for this composition is spherical. The size of the ZnO NPs measured about 20–30 nm. The TEM image of ZnO/CuO@BVE NCs displays particles with oval morphologies, where copper oxide nanoparticles are situated on ZnO NPs. The presence of zinc oxide nanoparticles attached to copper oxide particles is clearly discernible

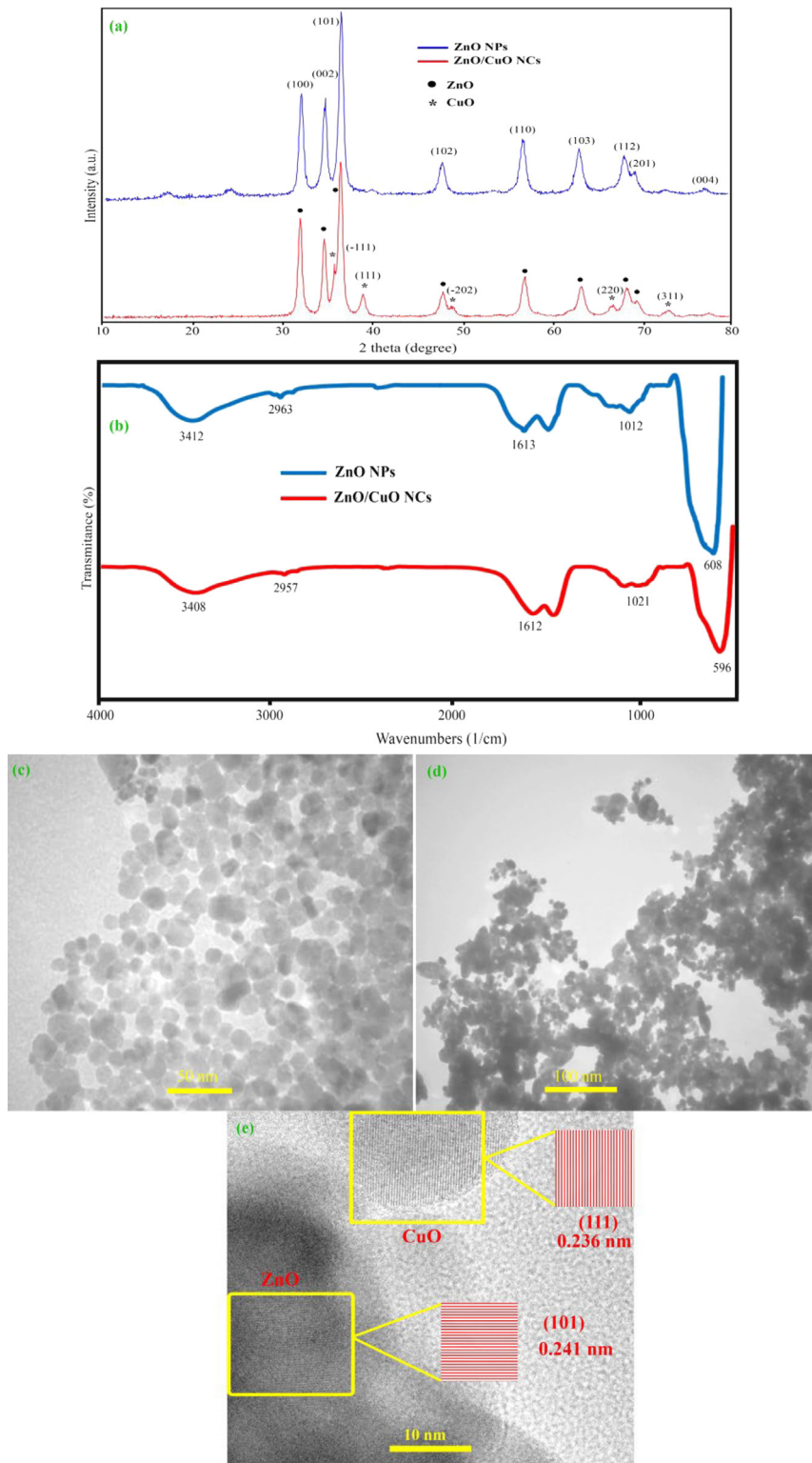


Fig. 1. (a) XRD pattern, (b) FT-IR analysis, TEM images of ZnO (c) and ZnO/CuO@BVE NCs (d), and HR-TEM image of ZnO/CuO@BVE NCs (e).

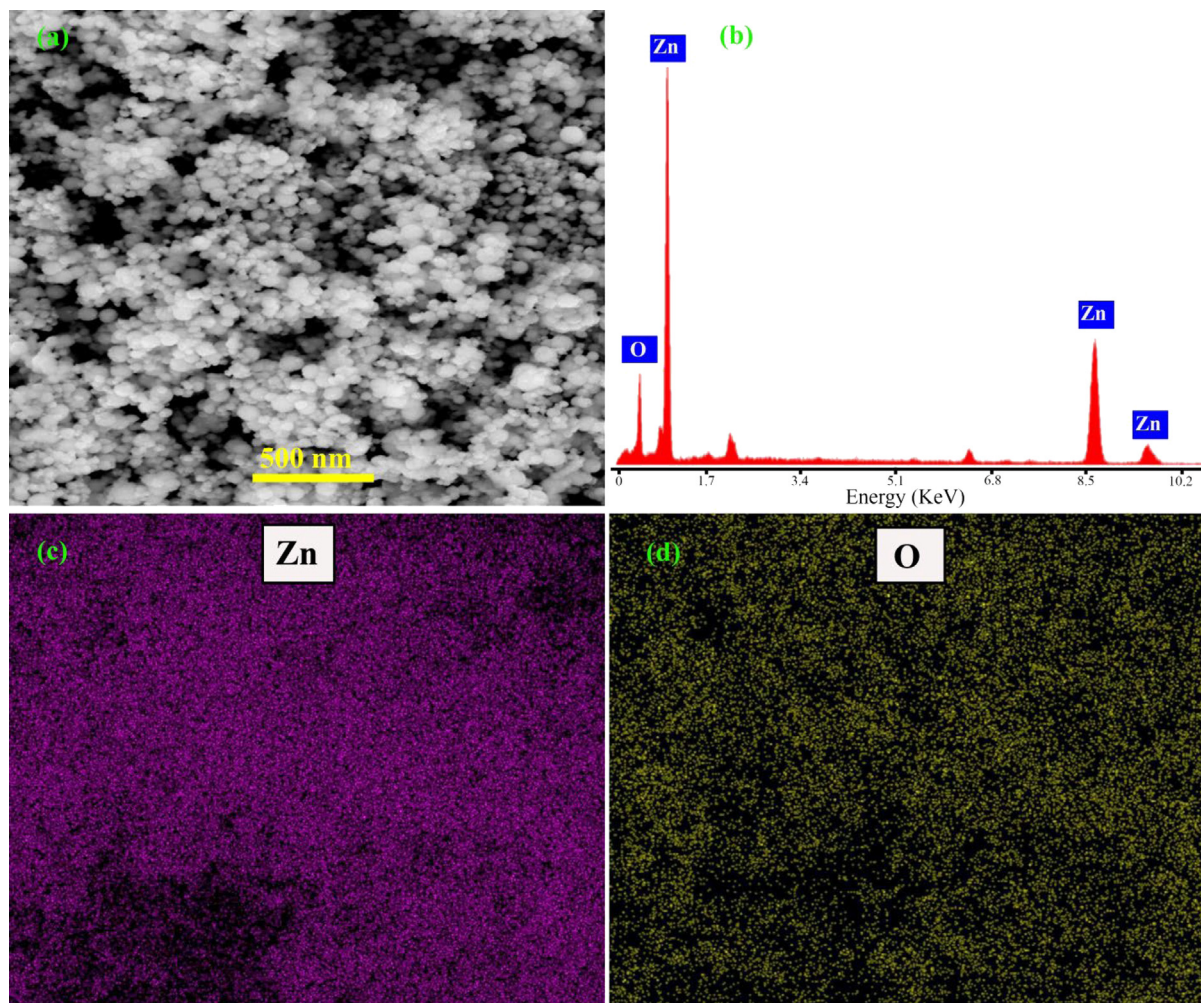


Fig. 2. FESEM image of (a), EDAX spectrum (b), and elemental mapping (c and d) of ZnO NPs.

in the ZnO/CuO@BVE NCs (as shown in Fig. 1e). The ZnO/CuO nanocomposites exhibit particles of varying sizes that are distinctly distinguishable in the TEM image. The average sizes of the particles ranged between 35 and 50 nm. The divergence in morphology of these particles compared to ZnO nanoparticles could be attributed to several factors, one of which is the difference in electronegativity between Zn^{2+} and Cu^{2+} ions (Jan et al., 2019). By analyzing the specifics presented in Fig. 1e, we can observe zinc oxide nanoparticles exhibiting a crystal plane orientation of (101) and a lattice spacing measuring 0.241 nm. Additionally, adjacent to these, copper oxide nanoparticles are positioned on the zinc oxide nanoparticles, characterized by a crystal plane orientation of (111) and a lattice spacing measuring 0.236 nm. The lattice spacing measurements for both of these compounds as observed in the HR-TEM spectrum align coherently with the interfacial spacing values depicted in their XRD pattern. Importantly, it should be highlighted that the existence of imperfections along the edges may arise from interplay among coupled phenomena (Thatikayala and Min, 2021).

3.2. FESEM and EDAX analysis

FESEM was employed to examine the shape and size of the synthesized samples. Figs. 2 and 3 illustrate the FESEM and EDAX micrographs of the pure ZnO NPs and ZnO/CuO@BVE NCs, respectively. Upon closer examination of the images, it becomes apparent that the pure zinc oxide nanoparticles exhibit a quasi-spherical morphology, remarkable uniformity, and a size of approximately 20–40 nm. However, following the deposition of copper oxide onto the surface of zinc oxide, variations in the compositions uniformity become evident, along with instances of adhesion in specific regions. In Fig. 3a and b, FESEM images show semi-spheroidal nanoparticles with irregular morphology, indicating that the ZnO/CuO@BVE NCs lack a specific morphology. EDAX analysis was employed to study the elemental composition of the surfaces of ZnO (as shown in Fig. 2b) and ZnO/CuO@BVE NCs (as depicted in Fig. 3c). The results reveal the presence of only Zn

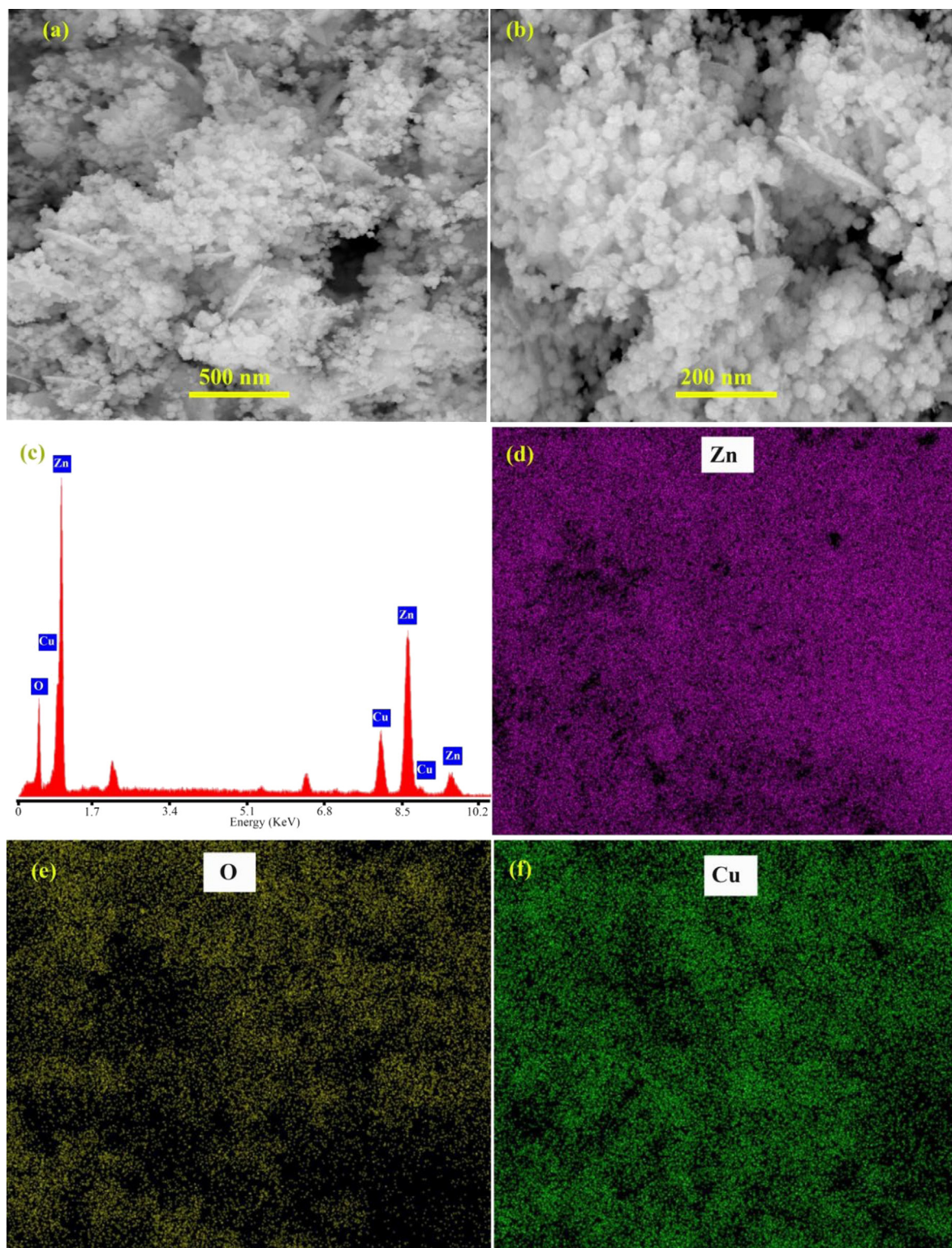


Fig. 3. FESEM images (a and b), EDAX spectrum (c), and elemental mapping (d-f) of ZnO/CuO@BVE NCs.

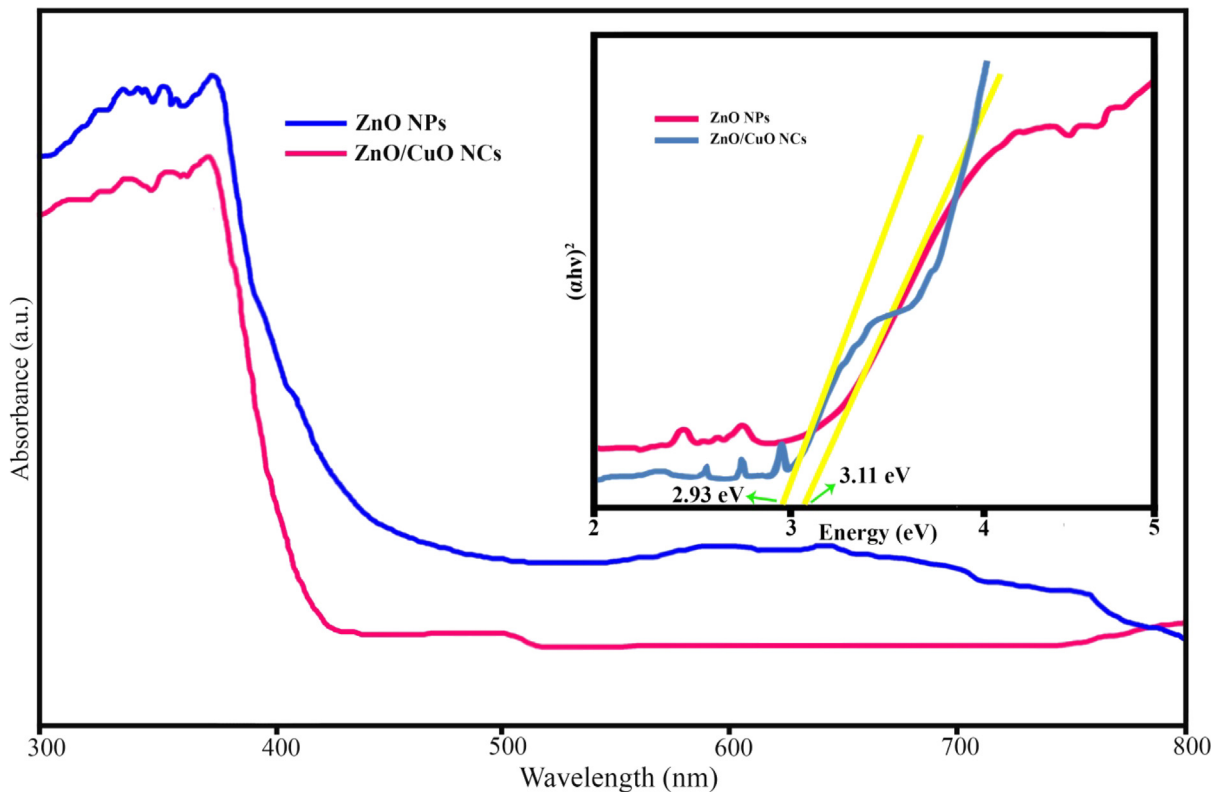


Fig. 4. UV-Vis DRS of ZnO NPs and ZnO/CuO@BVE NCs.

and O elements in the pure ZnO nanoparticles, with no impurities. Similarly, the corresponding EDAX spectrum of the ZnO/CuO@BVE NCs confirms the presence of oxygen, zinc, and copper elements. The outcomes of the EDAX analysis are consistent with the research findings of Kumari and her colleagues (Kumari et al., 2020). Furthermore, Khandaker and his research team successfully produced nanoparticles composed of copper oxide and zinc oxide through the utilization of *Coriandrum sativum* extract. EDAX analysis revealed prominent signals corresponding to oxygen, zinc, and copper elements, prominently appearing within the energy range of 1 to 8–10 KeV (Basit et al., 2023). Hence, our findings align entirely with the outcomes documented by previous investigators in this field.

3.3. Optical properties

UV-Vis spectra were utilized to investigate the optical properties of the prepared pure ZnO nanoparticles and ZnO/CuO@BVE NCs. These spectra are displayed in Fig. 4. The UV-Vis analysis revealed a strong absorption peak at 386 nm for pure ZnO, while in the ZnO/CuO@BVE NCs, an absorption band was observed at 392 nm. The maximum absorption wavelength of the ZnO/CuO@BVE NCs was red-shifted comparison to pure ZnO. This shift can be attributed to the integration of CuO, as well as increased surface defects and oxygen vacancies (Meena et al., 2021). Tauc plots were employed to determine the bandgap of pure ZnO and, ZnO/CuO@BVE NCs, and the results are illustrated in Fig. 4 (Javadmoosavi et al., 2023). The energy band gap was calculated as 3.11 eV for ZnO and 2.93 eV for ZnO/CuO@BVE NCs. This indicates that ZnO/CuO@BVE NCs have the capability to absorb both UV and visible light, making them promising candidates for solar-driven photocatalytic applications. The obtained energy gap value of 2.93 eV was consistent with the values reported for ZnO/CuO@BVE NCs in previous studies. For instance, Singh et al. reported an E_g of 3.16 eV for CuO nanoparticles modified ZnO (Singh and Soni, 2020). Variations in particle size and distribution, induced by the influence of quantum confinement, can account for alterations in the band gap energy of nanomaterials. Moreover, shifts in the optical band gap energy are attributed to additional factors such as structural anomalies within layers and modifications occurring at the interfaces of zinc oxide and copper oxide grains. The outcomes of our optical bandgap measurements for ZnO/CuO@BVE NCs are consistent with those reported by Maru et al. (2023).

Table 1
Antibacterial potential of the synthesized ZnO/CuO@BVE NCs against various bacteria.

Bacterial	Extract	ZnO/CuO@BVE NCs	
	MIC ($\mu\text{g/mL}$)	MIC ($\mu\text{g/mL}$)	MBC ($\mu\text{g/mL}$)
<i>S. aureus</i> ATCC 29213	>4000	500	1000
<i>S. epidermidis</i> ATCC 12228	>4000	125	500
<i>E. faecalis</i> ATCC 29212	>4000	250	500
<i>E. coli</i> ATCC 25922	>4000	125	500
<i>P. aeruginosa</i> ATCC27853	>4000	62.5	250
<i>K. pneumoniae</i> ATCC 9997	>4000	62.5	125

Table 2
Antifungal activity of ZnO/CuO@BVE NCs.

Fungus	ZnO/CuO@BVE NCs	
	MIC ($\mu\text{g/mL}$)	MFC ($\mu\text{g/mL}$)
<i>C. albicans</i> ATCC 10231	31.2	125

3.4. Antibacterial and antifungal activities

Tables 1 and 2 present the outcomes of antibacterial and antifungal investigations using *B. vulgaris* extract and ZnO/CuO@BVE NCs, respectively. Based on the antibacterial findings, ZnO/CuO@BVE NCs exhibited outstanding antibacterial effectiveness, showing a stronger impact on Gram-negative bacteria compared to Gram-positive bacteria. The study revealed high antibacterial performance against *P. aeruginosa* and *K. pneumonia* (MIC = 62.5 $\mu\text{g/mL}$). On the other hand, *S. aureus* (MIC = 500 $\mu\text{g/mL}$) and *E. faecalis* (MIC = 250 $\mu\text{g/mL}$) demonstrated the lowest antibacterial efficacy. Nanomaterials have the potential to penetrate the bacterial membrane more effectively and kill them due to the thinner layer surrounding Gram-negative bacteria and the presence of a lipopolysaccharide layer surrounding their membrane (Behravan et al., 2019). The results of the study indicated that ZnO/CuO@BVE NCs are more efficient against *C. albicans* compared to bacteria. The results can be explained by the distinction between eukaryotic fungi and prokaryotic bacteria (Marulasiddeshwara et al., 2017). The antibacterial mechanism of nanomaterials is not yet fully understood. Nanomaterials shape and size are generally associated with their antibacterial activity. Fig. S1 illustrates the proposed mechanism of antibacterial activity. When nanomaterials are smaller, they possess a larger surface area to their volume, increasing the likelihood of them attaching to the microorganism and causing an effect (Soleimani et al., 2018). Due to their small size, nanomaterials can penetrate bacteria and interfere with their functions by attaching to functional domains of vital proteins and binding to nucleic acids. Furthermore, they can induce oxidative stress in microorganisms and modify the activity of crucial microbial proteins. As these disruptions accumulate in microorganisms, their membrane function and permeability may be altered, ultimately leading to their destruction (Dangi et al., 2020). Because copper ions are highly reactive and possess significant bactericidal capabilities, the incorporation of copper oxide into zinc oxide composites results in the most potent antibacterial impact, primarily driven by the liberation of copper ions. Notably, antibacterial efficacy is heightened when the crystal size is reduced. This correlation arises from the fact that the ionic radius of copper ions is smaller than that of zinc ions, contributing to enhanced antibacterial activity (Liau and Huang, 2017).

3.5. Photocatalytic activity

Rhodamine B was utilized as a contaminant to assess the photocatalytic efficiency of the synthesized nanocomposites under UV light exposure. Past studies (Javadmoosavi et al., 2023) have demonstrated that the degradation of pollutants can be influenced by various factors, such as pH, nanocatalyst dosage, and exposure time. Thus, this study investigated the effects of pH, nanocatalyst dosage, light source, and pollutant concentration on the degradation of rhodamine B.

3.5.1. Effect of pH

The experiment involved adjusting the pH of the pollutant solution to examine the impact of pH values (3, 5, 7, 9, and 11) on the degradation of rhodamine B (Fig. 5a). The concentration of the contaminant solution used in the experiment was 5 ppm, and the nanocatalyst dosage (ZnO/CuO@BVE NCs) was set at 0.1 g/L. The reaction was conducted under UV light irradiation, and the pH was adjusted using solutions of NaOH and HCl. The results revealed that the highest absorption percentage was 25.05% when the pH was set to 3, following a 30-minute period of darkness. Moreover, the results showed an increase in the percentage of rhodamine B decomposition from 59.42% at pH 3 to 66.94% at pH 5. The degradation process of rhodamine B ceased at pH 7, resulting in the lowest percentage of pollutant degradation (58.5%). However, the degradation efficiency improved as the pH increased from 3 to 11, reaching the highest absorption percentage at pH 11 (74.94%). With an increase in pH, the concentration of OH ions rises, leading to a higher generation of OH radicals. Hydroxyl radicals are known for their high reactivity, effectively breaking down pollutants and thus yielding greater degradation efficiency at higher pH levels (Byrappa et al., 2006; Jain and Shrivastava, 2008). Consequently, the optimal pH for pollutant degradation was identified as 11. In pH 3, the HO_2 can form H_2O_2 , leading to the creation of the hydroxyl radical. As pH

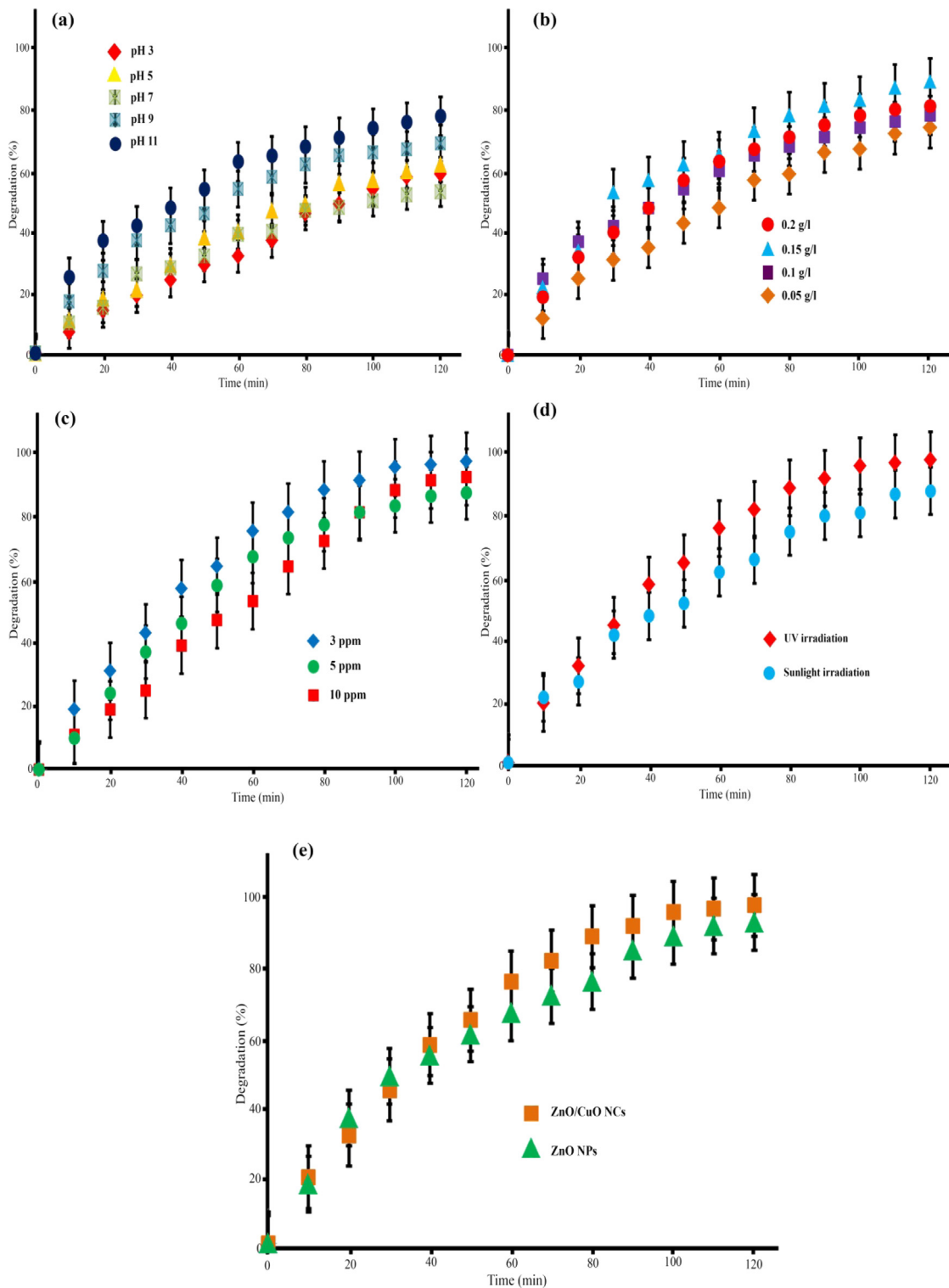


Fig. 5. Effect of pH (a), initial nanocatalyst concentration (b), dye solution concentration (c), various irradiations (d), and various nanocatalyst (e) on degradation of rhodamine b.

deviates from 7, whether increasing or decreasing, the reaction rate escalates due to the initiation of the decomposition reaction by formed OH radicals. Wilhelm and Stephan reported that in the absence of nanocomposite, the photocatalytic

decomposition mechanism of rhodamine B follows these reactions (Wilhelm and Stephan, 2007):



3.5.2. Influence of nanocatalyst dosage

To investigate the influence of ZnO/CuO@BVE NCs dose on the removal rate rhodamine B, varying amounts of the adsorbent (ranging from 0.05 to 0.2 g/L) were introduced to the rhodamine B solution (Fig. 5b). The results from the spectrophotometer indicated that the optimal removal occurred at a ZnO/CuO@BVE NCs dose of 0.15 g/L, achieving a removal percentage of 85.14%. However, when the nanocomposite dose was increased to 0.2 g/L, the decomposition of rhodamine B dropped to 71.22%, denoting a removal rate lower than that seen with the optimal dose of 0.15 g/L. The decline in decomposition efficiency can be attributed to the heightened concentration of the nanocomposite, culminating in increased turbidity. This, in turn, reduces the light's ability to penetrate the solution, leading to a diminished efficiency in photocatalytic degradation. Light is dispersed and fails to adequately penetrate the solution's depth, leading to fewer activated sites (Pouretedal et al., 2009). The outcomes of this research resonate with the findings presented by Khodadadi et al. (2018). The results demonstrated that as the dose of the nanocatalyst increased, the count of active sites on the nanocatalyst surface also amplified, leading to an accelerated rate of pollutant decomposition. This observation was paralleled in the research conducted by Xiaoqing Chen. An escalation in the nanocatalyst quantity resulted in an increased number of active sites on its surface, further leading to a surge in radical formation (Chen et al., 2017). However, it is also noteworthy that with an increase in the dose of nanocatalysts, these compounds tend to agglomerate, thereby restricting photons from accessing the active sites of the materials.

3.5.3. Influence of dye solution

To investigate the influence of dye concentration on the removal of rhodamine B dye using ZnO/CuO@BVE NCs, solutions were prepared with pollutant concentrations of 10 ppm, 5 ppm, and 3 ppm were prepared (Fig. 5c). The adsorbent dose was held constant at 0.15 gr/l, and the pH was adjusted to 11. The results revealed that the efficiency of rhodamine B decomposition decreased with increasing dye concentration. The highest percentage was observed at a concentration of 3 ppm, while the removal percentages at 5 ppm and 10 ppm were lower. Specifically, the removal percentages were 97.3% at 3 ppm, 90.13% at 5 ppm, and 83.62% at 10 ppm dye concentration. Similar outcomes were obtained in the study conducted by K. Byrappa and colleagues (Byrappa et al., 2006). The active surface of the catalyst plays a crucial role in the degradation reaction, as an increase in the initial amount of rhodamine B dye resulted in reduced performance. At a higher concentrations, the path length of photons entering the solution shortened, leading to negligible photocatalytic degradation (Byrappa et al., 2006). It is possible that the occupation of active sites by rhodamine B molecules at high concentrations could reduce decomposition efficiency. This limitation could restrict the number of available active sites for the reaction, resulting in fewer reactions and reduced efficiency. Similar findings were observed in the study by Chen et al. (2017). The rate of color removal decreased at higher concentrations.

3.5.4. Effect of light source

In the previous step, we determined the optimal parameters for pH, catalyst dosage, and dye solution. In this stage, we investigated the effects of different light sources, specifically UV and sunlight, on the decomposition of rhodamine B (Fig. 5d). It is widely recognized that the degradation of the contaminant in the absence of any light source (in darkness) was negligible, with only a 3.38% degradation observed. Therefore, these results can be disregarded. Under UV irradiation, the decomposition of rhodamine B using ZnO/CuO@BVE NCs reached 97.3% within 120 min. Furthermore, we examined the decomposition of rhodamine b in sunlight conditions, which demonstrated approximately 81.7% photodegradation. This increase in the photocatalytic degradation efficiency of pollutants by ZnO/CuO@BVE NCs can be attributed to their low energy gap and enhanced absorption of visible light.

3.5.5. Comparison of efficiency of pure ZnO NPs and ZnO/CuO@BVE NCs

To compare the efficiency between pure ZnO NPs and ZnO/CuO@BVE NCs, we examined the role of copper oxide in the degradation of the rhodamine B pollutant (Fig. 5e). The optimal degradation conditions were determined for zinc oxide nanoparticles, which included a pH of 11, dye solution concentration of 3 ppm, and nanocatalyst dosage of 0.15 g/L. The data showed that zinc oxide nanoparticles achieved a degradation rate of 89.5% for the rhodamine B pollutant after 120 min. A comparative evaluation suggests that the inclusion of copper oxide nanoparticles in ZnO/CuO@BVE NCs markedly improved the pollutant degradation efficiency.

3.5.6. Photocatalytic degradation mechanism

Multiple steps and processes contribute to the subsequent decomposition mechanism, as depicted in Fig. S2. (Chang et al., 2013). The band structure and charge transfer process of ZnO/CuO@BVE NCs play a crucial role in the photocatalytic decomposition. Under UV light exposure, ZnO absorbs photons, generating photo-induced electron-hole pairs. Electrons are excited to the conduction band, while positive holes form in ZnO valence band. Dissolved oxygen adsorbed onto the ZnO surface facilitates electron reactions with oxygen, resulting in the formation of superoxide radicals ($O_2^{\cdot-}$). These highly reactive superoxide radicals contribute to RhB molecule degradation. In the band structure of ZnO/CuO@BVE NCs, the energy levels of ZnO and CuO allow the direct transfer of photo-induced holes from ZnO to CuO. This hole transfer minimizes electron-hole pair recombination, ensuring efficient utilization of the photo-induced charges. Photo-induced holes in ZnO are employed to oxidize hydroxide ions (OH^-) into hydroxyl radicals ($\cdot OH$), potent oxidizing species. These hydroxyl radicals drive the continuous degradation of RhB molecules into simpler organic compounds. The degradation advances as reactive oxidation species, including superoxide radicals and hydroxyl radicals, consistently react with dye molecules, breaking down complex dye molecules into smaller organic fragments. Ultimately, these degradation products are transformed into environmentally benign carbon dioxide (CO_2) and water (H_2O). The effective charge transfer between ZnO and CuO in ZnO/CuO@BVE NCs critically enhances the photocatalytic degradation process. Direct hole transfer from ZnO to CuO curbs charge recombination, enabling sustained photocatalytic activity and efficient RhB degradation.

4. Conclusion

ZnO/CuO nanocomposites were synthesized using *berberis vulgaris* extract. The resulting ZnO/CuO@BVE NCs exhibited a spherical shape. Notably, these nanocomposites demonstrated remarkable photocatalytic activity, achieving a degradation rate of 97.3% for rhodamine B dye within a 120 min. Moreover, the ZnO/CuO@BVE NCs displayed potent antifungal and antibacterial performance against six types of microorganisms. These distinctive characteristics of the synthesized nanocomposites underscore their cost-effective synthesis method, efficacy as photocatalysts, and potential applications in pharmaceutical wastewater treatment, as well as their utility as antifungal and antibacterial agents.

Declaration of competing interest

We accept all ethical responsibilities of authors and declare that authors have no conflict of interest. As well as, we declare that this manuscript has not been submitted elsewhere for publication and it is not under consideration for publication elsewhere. Furthermore, any illustration, structure or table has not been published elsewhere.

Data availability

Data will be made available on request.

Acknowledgment

This research is the result of research with ethical code IR.BUMS.REC.1400.121. We are grateful to Birjand University of Medical Sciences, Iran for supporting this research.

Appendix A. Supplementary data

Supplementary material related to this article can be found online at <https://doi.org/10.1016/j.eti.2023.103340>.

References

- Abdussalam-Mohammed, W., Qasem Ali, A., O. Errayes, A., 2020. Green chemistry: Principles applications, and disadvantages. *Chem. Methodol.* 4 (4), 408–423.
- Anzabi, Y., 2018. Biosynthesis of ZnO nanoparticles using barberry (*Berberis vulgaris*) extract and assessment of their physico-chemical properties and antibacterial activities. *Green Process. Synth.* 7 (2), 114–121.
- Bader, N., Hasan, H., EL-Denali, A., 2018. Determination of Cu Co, and Pb in selected frozen fish tissues collected from Benghazi markets in Libya. *Chemical Methodologies* 2 (1), 56–63.
- Baldez, E.E., Robaina, N.F., Cassella, R.J., 2008. Employment of polyurethane foam for the adsorption of Methylene Blue in aqueous medium. *J. Hazard. Mater.* 159 (2), 580–586.
- Basit, R.A., Abbasi, Z., Hafeez, M., Ahmad, P., Khan, J., Khandaker, M.U., Al-Mugren, K.S., Khalid, A., 2023. Successive photocatalytic degradation of methylene blue by ZnO CuO and ZnO/CuO synthesized from coriandrum sativum plant extract via green synthesis technique. *Crystals* 13 (2), 281.
- Behravan, M., Panahi, A.Hosseini, Naghizadeh, A., Ziaee, M., Mahdavi, R., Mirzapour, A., 2019. Facile green synthesis of silver nanoparticles using *Berberis vulgaris* leaf and root aqueous extract and its antibacterial activity. *Int. J. Biol. Macromol.* 124, 148–154.
- Byrappa, K., Subramani, A.K., Ananda, S., Rai, K.M.L., Dinesh, R., Yoshimura, M., 2006. Photocatalytic degradation of rhodamine B dye using hydrothermally synthesized ZnO. *Bull. Mater. Sci.* 29 (5), 433–438.
- Cao, Y., Dhahad, H.A., El-Shorbagy, M.A., Aljani, H.Q., Zakeri, M., Heydari, A., Bahonar, E., Slouf, M., Khatami, M., Naderifar, M., Iravani, S., Khatami, S., Dehkordi, F.F., 2021. Green synthesis of bimetallic ZnO–CuO nanoparticles and their cytotoxicity properties. *Sci. Rep.* 11 (1), 23479.

- Ceril Jeffrey, A., Jothi Ramalingam, S., Murugaiah, K., Balu, A.R., 2023. One-pot green synthesis of rGO-NiO/CdO nanocomposite materials for the photocatalytic degradation of phenol from waste waters and the study of resistance against staphylococcus aureus. *Hybrid Adv.* 3, 100064.
- Chang, T., Li, Z., Yun, G., Jia, Y., Yang, H., 2013. Enhanced photocatalytic activity of ZnO/CuO nanocomposites synthesized by hydrothermal method. *Nano-Micro Letters* 5 (3), 163–168.
- Chen, X., Wu, Z., Liu, D., Gao, Z., 2017. Preparation of ZnO photocatalyst for the efficient and rapid photocatalytic degradation of azo dyes. *Nanoscale Research Letters* 12 (1), 143.
- Chong, M.N., Jin, B., Chow, C.W.K., Saint, C., 2010. Recent developments in photocatalytic water treatment technology: A review. *Water Res.* 44 (10), 2997–3027.
- Dangi, S., Gupta, A., Gupta, D.K., Singh, S., Parajuli, N., 2020. Green synthesis of silver nanoparticles using aqueous root extract of berberis asiatica and evaluation of their antibacterial activity. *Chemical Data Collections* 28, 100411.
- Filipić, G., Cvelbar, U., 2012. Copper oxide nanowires: a review of growth. *Nanotechnology* 23 (19), 194001.
- Fouladi-Fard, R., Aali, R., Mohammadi-Aghdam, S., Mortazavi-Derazkola, S., 2022. The surface modification of spherical ZnO with Ag nanoparticles: A novel agent biogenic synthesis, catalytic and antibacterial activities. *Arab. J. Chem.* 15 (3), 103658.
- Golrizkhatami, F., Taghavi, L., Nasseh, N., Panahi, H.A., 2023. Synthesis of novel MnFe₂O₄/bio green nanocomposite and its application to photocatalytic degradation of tetracycline hydrochloride: (LC-MS analyses mechanism, reusability, kinetic, radical agents, mineralization, process capability, and purification of actual pharmaceutical wastewater). *J. Photochem. Photobiol. A Chem.* 444, 114989.
- Hashemi, Z., Mizwari, Z.M., Mohammadi-Aghdam, S., Mortazavi-Derazkola, S., Ali Ebrahimzadeh, M., 2022. Sustainable green synthesis of silver nanoparticles using sambucus ebulus phenolic extract (AgNPs@SEE): Optimization and assessment of photocatalytic degradation of methyl orange and their in vitro antibacterial and anticancer activity. *Arab. J. Chem.* 15 (1), 103525.
- Hermenean, A., Popescu, C., Ardelean, A., Stan, M., Hadaruga, N., Mihali, C.V., Costache, M., Dinischiotu, A., 2012. Hepatoprotective effects of berberis vulgaris L extract/ β cyclodextrin on carbon tetrachloride-induced acute toxicity in mice. *Int. J. Mol. Sci.* 13 (7), 9014–9034.
- Hoshyar, R., Mahboob, Z., Zarban, A., 2016. The antioxidant and chemical properties of *Berberis vulgaris* and its cytotoxic effect on human breast carcinoma cells. *Cytotechnology* 68 (4), 1207–1213.
- Hu, J.-z., Skrabal, P., Zollinger, H., 1987. A comparison of the absorption spectra of a series of blue disperse dyes with the colorimetric evaluation of their dyeings. *Dye. Pigment.* 8 (3), 189–209.
- Huang, J.-J., Hu, H.-Y., Tang, F., Li, Y., Lu, S.-Q., Lu, Y., 2011. Inactivation and reactivation of antibiotic-resistant bacteria by chlorination in secondary effluents of a municipal wastewater treatment plant. *Water Res.* 45 (9), 2775–2781.
- Huang, L.S., Yang, S.G., Li, T., Gu, B.X., Du, Y.W., Lu, Y.N., Shi, S.Z., 2004. Preparation of large-scale cupric oxide nanowires by thermal evaporation method. *J. Cryst. Growth* 260 (1), 130–135.
- Imenshahidi, M., Hosseinzadeh, H., 2016. *Berberis Vulgaris* and *Berberine*: An update review. *Phytotherapy Res.* PTR 30 (11), 1745–1764.
- Jafarirad, S., Mehrabi, M., Divband, B., Kosari-Nasab, M., 2016. Biofabrication of zinc oxide nanoparticles using fruit extract of *Rosa canina* and their toxic potential against bacteria: A mechanistic approach. *Mater. Sci. Eng. C* 59, 296–302.
- Jain, R., Shrivastava, M., 2008. Photocatalytic removal of hazardous dye cyanosine from industrial waste using titanium dioxide. *J. Hazard. Mater.* 152 (1), 216–220.
- Jan, T., Azmat, S., Mansoor, Q., Waqas, H.M., Adil, M., Ilyas, S.Z., Ahmad, I., Ismail, M., 2019. Superior antibacterial activity of ZnO-CuO nanocomposite synthesized by a chemical co-precipitation approach. *Microb. Pathogenesis* 134, 103579.
- Javadoosavi, S.Y., Naghizadeh, A., Mizwari, Z.M., Mortazavi-Derazkola, S., 2023. Biosynthesis of novel NiFe₂O₄-X (X=ZnO and TiO₂) magnetic nanophotocatalyst toward the degradation pharmaceutical ceftriaxone sodium from aqueous solution under sunlight irradiation and antibacterial activity. *Ceram. Int.* 49 (1), 1351–1361.
- Jayaprakash, J., Srinivasan, N., Chandrasekaran, P., Girija, E.K., 2015. Synthesis and characterization of cluster of grapes like pure and Zinc-doped CuO nanoparticles by sol-gel method. *Spectrochimica Acta Part A Mol. Biomol. Spectroscopy* 136, 1803–1806.
- Khan, S.B., Faisal, M., Rahman, M.M., Jamal, A., 2011. Low-temperature growth of ZnO nanoparticles: Photocatalyst and acetone sensor. *Talanta* 85 (2), 943–949.
- Khodadadi, M., Ehrampoush, M.H., Ghaneini, M.T., Allahresani, A., Mahvi, A.H., 2018. Synthesis and characterizations of FeNi₃@SiO₂@TiO₂ nanocomposite and its application in photo-catalytic degradation of tetracycline in simulated wastewater. *J. Mol. Liq.* 255, 224–232.
- Khormali, K., Mizwari, Z.M., Masoumeh Ghoreishi, S., Mortazavi-Derazkola, S., Khezri, B., 2021. Novel Dy₂O₃/ZnO-Au ternary nanocomposites: Green synthesis using pomegranate fruit extract characterization and their photocatalytic and antibacterial properties. *Bioorganic Chem.* 115, 105204.
- Kumari, V., Yadav, S., Jindal, J., Sharma, S., Kumari, K., Kumar, N., 2020. Synthesis and characterization of heterogeneous ZnO/CuO hierarchical nanostructures for photocatalytic degradation of organic pollutant. *Adv. Powder Technol.* 31 (7), 2658–2668.
- Li, D., Haneda, H., 2003. Morphologies of zinc oxide particles and their effects on photocatalysis. *Chemosphere* 51 (2), 129–137.
- Liau, L.C.-K., Huang, J.-S., 2017. Energy-level variations of Cu-doped ZnO fabricated through sol-gel processing. *J. Alloys Compd.* 702, 153–160.
- Lillo-Ramiro, J., Guerrero-Villalba, J.M., Mota-González, M.d. L., Tostado, F.S.A., Gutiérrez-Heredia, G., Mejía-Silva, I., Castillo, A.C., 2021. Optical and microstructural characteristics of CuO thin films by sol gel process and introducing in non-enzymatic glucose biosensor applications. *Optik* 229, 166238.
- Lv, Y., Liu, J., Zhang, Z., Zhang, W., Wang, A., Tian, F., Zhao, W., Yan, J., 2021. Green synthesis of CuO nanoparticles-loaded ZnO nanowires arrays with enhanced photocatalytic activity. *Mater. Chem. Phys.* 267, 124703.
- Maru, M.T., Gonfa, B.A., Zeleke, O.A., Fakrudeen, S.P., Ananda Murthy, H.C., Bekele, E.T., Sabir, F.K., 2023. Effect of *Musa acuminata* peel extract on synthesis of ZnO/CuO nanocomposites for photocatalytic degradation of methylene blue. *Green Chem. Lett. Rev.* 16 (1), 2232383.
- Marulasiddeshwara, M.B., Dakshayani, S.S., Sharath Kumar, M.N., Chethana, R., Raghavendra Kumar, P., Devaraja, S., 2017. Facile-one pot-green synthesis antibacterial, antifungal, antioxidant and antiplatelet activities of lignin capped silver nanoparticles: a promising therapeutic agent. *Mater. Sci. Eng. C* 81, 182–190.
- Meena, P.L., Surela, A.K., Poswal, K., 2021. Fabrication of ZnO/CuO hybrid nanocomposite for photocatalytic degradation of brilliant cresyl blue (BCB) dye in aqueous solutions. *J. Water Environ. Nanotechnol.* 6 (3), 196–211.
- Nagajyothi, P.C., Muthuraman, P., Sreekanth, T.V.M., Kim, D.H., Shim, J., 2017. Green synthesis: In-vitro anticancer activity of copper oxide nanoparticles against human cervical carcinoma cells. *Arab. J. Chem.* 10 (2), 215–225.
- Nguyen, N.T., Nguyen, N.T., Nguyen, V.A., 2020. In situ synthesis and characterization of ZnO/chitosan nanocomposite as an adsorbent for removal of Congo red from aqueous solution. *Adv. Polym. Technol.* 2020, 3892694.
- Ollis, D.F., 2018. Kinetics of photocatalyzed reactions: Five lessons learned. *Front. Chem.* 6 (378).
- Parekh, Z.R., Chaki, S.H., Hirpara, A.B., Patel, G.H., Kannaujia, R.M., Khimani, A.J., Deshpande, M.P., 2021. CuO nanoparticles – Synthesis by wet precipitation technique and its characterization. *Physica B* 610, 412950.
- Pouretedal, H.R., Norozi, A., Keshavarz, M.H., Semnani, A., 2009. Nanoparticles of zinc sulfide doped with manganese nickel and copper as nanophotocatalyst in the degradation of organic dyes. *J. Hazardous Mater.* 162 (2), 674–681.
- Roya Alizadeh, S., Nemati Seyghalan, H., Hashemi, Z., Ebrahimzadeh, M.Ali., 2023. *Scrophularia striata* extract mediated synthesis of gold nanoparticles; their antibacterial, antileishmanial, antioxidant, and photocatalytic activities. *Inorganic Chem. Commun.* 111138.

- Sadeghi, M., Farhadi, S., Zabardasti, A., 2020. Fabrication of a novel magnetic CdS nanorod/nife2o4/nax zeolite nanocomposite with enhanced sonocatalytic performance in the degradation of organic dyes. *New J. Chem.* 44 (20), 8386–8401.
- Sarentuya, Bai, H., Amurishana, 2023. Synthesis of Bi2S3-TiO2 nanocomposite and its electrochemical and enhanced photocatalytic properties for phenol degradation. *Int. J. Electrochem. Sci.* 18 (4), 100071.
- Senthil Kumar, P., Selvakumar, M., Ganesh Babu, S., Induja, S., Karuthapandian, S., 2017. CuO/ZnO nanorods: An affordable efficient p-n heterojunction and morphology dependent photocatalytic activity against organic contaminants. *J. Alloys Compd.* 701, 562–573.
- Shirzadi-Ahodashi, M., Mizwari, Z.M., Hashemi, Z., Rajabalipour, S., Ghoreishi, S.M., Mortazavi-Derazkola, S., Ebrahimzadeh, M.A., 2021. Discovery of high antibacterial and catalytic activities of biosynthesized silver nanoparticles using *C. fruticulosus* (CF-AgNPs) against multi-drug resistant clinical strains and hazardous pollutants. *Environ. Technol. Innov.* 23, 101607.
- Shokraiyani, J., Asadi, M., Rabbani, M., 2021. A comparison of photocatalytic activity of CuO ZnO, and ZnO/CuO nanocomposites for degrading water pollutants under LED light. *Chem. Data Collect.* 34, 100747.
- Singh, J., Soni, R.K., 2020. Controlled synthesis of CuO decorated defect enriched ZnO nanoflakes for improved sunlight-induced photocatalytic degradation of organic pollutants. *Appl. Surf. Sci.* 521, 146420.
- Soleimani, F.F., Saleh, T., Shojaosadati, S.A., Poursalehi, R., 2018. Green synthesis of different shapes of silver nanostructures and evaluation of their antibacterial and cytotoxic activity. *BioNanoScience* 8 (1), 72–80.
- Srivastava, S., Srivastava, M., Misra, A., Pandey, G., Rawat, A., 2015. A review on biological and chemical diversity in *Berberis* (Berberidaceae). *EXCLI J.* 14, 247–267.
- Sun, C., Fu, Y., Wang, Q., Xing, L., Liu, B., Xue, X., 2016. Ultrafast piezo-photocatalytic degradation of organic pollutions by Ag2O/tetrapod-ZnO nanostructures under ultrasonic/UV exposure. *RSC Adv.* 6 (90), 87446–87453.
- Thatikayala, D., Min, B., 2021. Ginkgo leaves extract-assisted synthesis of ZnO/CuO nanocrystals for efficient UV-induced photodegradation of organic dyes and antibacterial activity. *J. Mater. Sci., Mater. Electron.* 32 (13), 17154–17169.
- Wang, J., Fan, X.M., Wu, D.Z., Dai, J., Liu, H., Liu, H.R., Zhou, Z.W., 2011. Fabrication of CuO/T-ZnOw nanocomposites using photo-deposition and their photocatalytic property. *Appl. Surf. Sci.* 258 (5), 1797–1805.
- Wilhelm, P., Stephan, D., 2007. Photodegradation of rhodamine B in aqueous solution via SiO2@TiO2 nano-spheres. *J. Photochem. Photobiol. A Chem.* 185 (1), 19–25.
- Zaimbashi, R., Shampur, T., Mostafavi, A., 2022. Hydrothermal synthesis of ZnO nanoflowers for rapid detection of sertraline and imipramine using the modified screen-printed electrode. *J. Mater. Sci., Mater. Electron.* 33 (25), 19711–19722.
- Zeng, Z., Garoufalis, C.S., Terzis, A.F., Baskoutas, S., 2013. Linear and nonlinear optical properties of ZnO/ZnS and ZnS/ZnO core shell quantum dots: Effects of shell thickness, impurity, and dielectric environment. *J. Appl. Phys.* 114 (2).
- Zhu, L., Li, H., Liu, Z., Xia, P., Xie, Y., Xiong, D., 2018. Synthesis of the 0D/3D CuO/ZnO heterojunction with enhanced photocatalytic activity. *J. Phys. Chem. C* 122 (17), 9531–9539.